The Astronomical Journal, 150:85 (11pp), 2015 September doi:10.1088/0004-6256/150/3/85

HAT-P-56b: AN INFLATED MASSIVE HOT JUPITER TRANSITING A BRIGHT F STAR FOLLOWED UP WITH *K2* CAMPAIGN 0 OBSERVATIONS*

C. X. Huang[1], J. D. Hartman[1], G. Á. Bakos[1,6,7], K. Penev[1], W. Bhatti[1], A. Bieryla[2], M. de Val-Borro[1], D. W. Latham[2], L. A. Buchhave[2,3], Z. Csubry[1], G. Kovács[4], B. Béky[2], E. Falco[2], P. Berlind[2], M. L. Calkins[2], G. A. Esquerdo[2], J. Lázár[5], I. Papp[5], and P. Sári[5]

[1] Department of Astrophysical Sciences, Princeton University, Princeton, NJ 08544, USA; chelsea@astro.princeton.edu
[2] Harvard-Smithsonian Center for Astrophysics, Cambridge, MA 02138 USA; abieryla@cfa.harvard.edu
[3] Centre for Star and Planet Formation, Natural History Museum of Denmark, University of Copenhagen, DK-1350 Copenhagen, Denmark
[4] Konkoly Observatory, Budapest, Hungary
[5] Hungarian Astronomical Association (HAA), Hungary
Received 2015 June 4; accepted 2015 July 14; published 2015 August 25

ABSTRACT

We report the discovery of HAT-P-56b by the HATNet survey, an inflated hot Jupiter transiting a bright F-type star in Field 0 of NASA's *K2* mission. We combine ground-based discovery and follow-up light curves with high precision photometry from *K2*, as well as ground-based radial velocities from the Tillinghast Reflector Echelle Spectrograph on the Fred Lawrence Whipple Observatory 1.5 m telescope to determine the physical properties of this system. HAT-P-56b has a mass of 2.18 M_J, radius of 1.47 R_J, and transits its host star on a near-grazing orbit with a period of 2.7908 day. The radius of HAT-P-56b is among the largest known for a planet with $M_p > 2\ M_J$. The host star has a *V*-band magnitude of 10.9, mass of 1.30 $M_\odot$, and radius of 1.43 $R_\odot$. The periodogram of the *K2* light curve suggests that the star is a γ Dor variable. HAT-P-56b is an example of a ground-based discovery of a transiting planet, where space-based observations greatly improve the confidence in the confirmation of its planetary nature, and also improve the accuracy of the planetary parameters.

Key words: planetary systems – stars: individual (HAT-P-56) – techniques: photometric – techniques: spectroscopic

Supporting material: machine-readable and VO table

1. INTRODUCTION

Searching for transits is one of the most productive methods of detecting planets outside of our solar system. Transiting exoplanets (TEPs) around bright stars are of particular interest as they are the best targets for follow-up observations to investigate their detailed orbital geometries, atmospheric properties, and chemical compositions.

Recent years have seen a rapid increase in the discovery rate of transit exoplanets (TEPs). The *Kepler* Mission (Borucki et al. 2009) has identified ~4000 planetary candidates in its four years of operations (Mullally et al. 2015). Approximately 100 of the *Kepler* planets have had their mass measured using stellar radial velocities (Batalha et al. 2011, Gautier et al. 2012, Marcy et al. 2014, and many others), or numerically modeled transit timing variations (Lissauer et al. 2011, Carter et al. 2012, Wu & Lithwick 2013, and many others). The majority of *Kepler* planet candidate hosting stars are, however, often faint, complicating both the accurate planetary mass measurements and also the study of their physical nature. For example, to date, the majority of the planets with precise mass measurements are still from the ground-based wide field transiting planet surveys such as SuperWASP (Pollacco et al. 2006), HATNet/HATSouth (Bakos et al. 2004, 2013), KELT (Pepper et al. 2007), and others.

Traditionally, confirmation of planets from ground-based transit surveys relies on high precision photometric follow-up from one or two meter class ground-based telescopes. These follow-up observations ensure the robustness of the detections, help to rule out false positives due to binaries, and further constrain the planet parameters. However, due to the constraints of ground-based observations, it is usually difficult to observe the full orbital phase of a transiting planet candidate, including primary and secondary transits. The presence or lack of deep secondary eclipses, or out-of-transit variations is often important information for ruling out blended stellar eclipsing binary scenarios. The quality of ground-based photometry may also be reduced due to poor weather conditions, site and target restrictions, and airmass trends.

Due to the loss of two reaction wheels during the main mission, the *Kepler* spacecraft entered a new observation phase. This successor mission of *Kepler*, called the *K2* mission (Howell et al. 2014), covers a much larger area of sky with a step and stare strategy. The Guest Observation mode of this mission provides a great tool to follow up the ground-based planetary candidates, and enables a new method of discovering TEPs through a synergy between ground- and space-based transit surveys. *K2* observations allow us to obtain high precision light curves of candidates over a continuous and relatively long time-baseline covering many transit events due to a planet.

Once the planet is confirmed, having high precision light curves from space observations will also enable further

* Based on observations obtained with the Hungarian-made Automated Telescope Network. Based in part on observations obtained with the Tillinghast Reflector 1.5 m telescope and the 1.2 m telescope, both operated by the Smithsonian Astrophysical Observatory at the Fred Lawrence Whipple Observatory in Arizona. Based in part on observations obtained with the Apache Point Observatory 3.5 m telescope, which is owned and operated by the Astrophysical Research Consortium. Based in part on observations obtained with the *Kepler* Space Craft in the *K2* Campaign 0 Mission.
[6] Sloan Fellow.
[7] Packard Fellow.

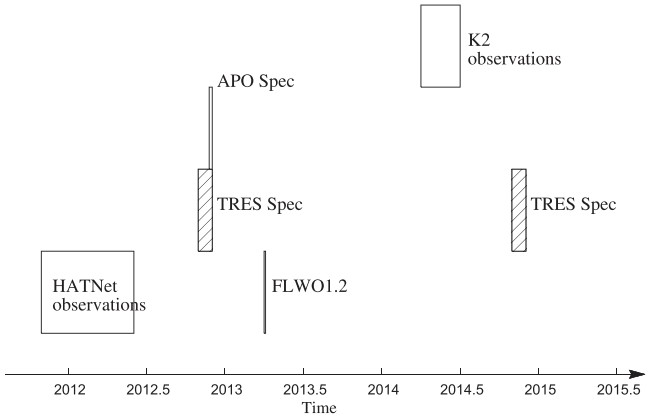

Figure 1. Sequence of observations that lead to the discovery and confirmation flow of HAT-P-56b.

characterization of the planet. Confirmed planets from the ground have been recognized as valuable targets to be followed up by *K2* (Brown et al. 2014; Bakos et al. 2015). The planets discovered by ground based TEP surveys, and also observed by the original *Kepler* Mission, such as TrEs-2b (O'Donovan et al. 2006), HAT-P-7b (Pál et al. 2008), and HAT-P-11b (Bakos et al. 2010), are among the best studied planets. With the high precision *Kepler* light curves, many effects due to the planets can be measured, such as the orbital phase variation and occultation of the planet (Borucki et al. 2009; Welsh et al. 2010; Kipping & Bakos 2011b; Barclay et al. 2012; Jackson et al. 2012). The spin–orbit obliquity angle of HAT-P-11b has also been constrained using the starspot crossing events observed in the *Kepler* light curves (Sanchis-Ojeda & Winn 2011; Deming et al. 2011). Detailed modeling of the transit shape using the Short Cadence photometry of *Kepler* can also be used to determine the probable gravity darkening effect, and constrain the oblateness of the planet (Morris et al. 2013; Zhu et al. 2014; Masuda 2015).

Following up candidates from ground-based transit surveys is an efficient way to utilize the *K2* observational resources. Due to constraints from the new mode of operation, the number of targets observed by *K2* per field is much smaller than for the original *Kepler* field. The high priority planetary candidates from ground-based surveys are pre-selected targets which are known to show transits, and which have already been vetted against various false positive scenarios. Selecting these candidates to fall on *K2* "postage stamps" is one way to increase the confirmed planet yield from this mission.

In this paper we present the discovery (see Figure 1) of a transiting planet, HAT-P-56b, in the *K2* Campaign 0 field. This planet was originally identified as a HATNet (Bakos et al. 2004) planetary candidate, was followed up by the Tillinghast Reflector Echelle Spectrograph (TRES) spectrograph on the Fred Lawrence Whipple Observatory (FLWO) 1.5 m telescope, and also by the KeplerCam imager on the FLWO 1.2 m telescope. Encouraged by these initial results, all pointing toward a bona fide planet orbiting the host star HAT-P-56, the target was proposed for *K2* observations. Indeed, the very high quality photometric observations of *K2* confirmed the transit, and also eliminated most of the possible blend scenarios. We then continued following-up HAT-P-56 with the TRES spectrograph, so as to determine the mass of the orbiting body.

Table 1
Differential Photometry of HAT-P-56

BJD[a] (2,400,000+)	Phot[b]	$\sigma_{\rm Phot}$	Phot(orig)[c]	Filter	Instrument
55954.98325	0.00245	0.00430	⋯	*r*	HATNet
55971.72852	0.00273	0.00463	⋯	*r*	HATNet
55860.09538	0.00383	0.00396	⋯	*r*	HATNet
55957.77449	0.00368	0.00464	⋯	*r*	HATNet
55929.86619	0.00725	0.00426	⋯	*r*	HATNet
55901.95813	−0.00271	0.00432	⋯	*r*	HATNet
55888.00414	−0.01589	0.00408	⋯	*r*	HATNet
55904.75041	0.00110	0.00603	⋯	*r*	HATNet
55929.86812	0.00151	0.00373	⋯	*r*	HATNet
55901.95982	0.00766	0.00400	⋯	*r*	HATNet

Notes.
[a] Barycentric Julian Date calculated directly from UTC, *without* correction for leap seconds for HATNet and KeplerCam.
[b] For HATNet and KeplerCam this is in units of magnitudes, for *K2* it is in relative flux. The out-of-transit level has been subtracted. These values have been corrected for trends simultaneously with the transit fit for the follow-up data. For HATNet trends were filtered *before* fitting for the transit.
[c] Raw photometry values after correction using comparison stars, but without additional trend-filtering. For KeplerCam this is in magnitudes, for *K2* it is in relative flux. We do not report this value for HATNet.

(This table is available in its entirety in machine-readable and Virtual Observatory (VO) forms.)

In Section 2 we summarize the detection of the photometric transit signal in the HATNet light curve, follow-up photometry from the ground and from *K2* campaign 0, and our spectroscopic follow-up. Analyses of the results are presented in Section 3. We show in Section 4 that HAT-P-56b is one of the most inflated objects observed that belong to the massive hot Jupiter population ($M > 2M_J$), even when we take into account of the amount of irradiation from the host star.

2. OBSERVATIONS

2.1. Ground Based Photometry

All time-series photometric data that we collected for HAT-P-56 are provided in Table 1. We discuss these observations below. All of our discovery data and follow-up data are publicly available in electronic format as machine readable tables, and also via HATNet website.[8]

2.1.1. Photometric Detection

The star HAT-P-56 was observed by the HATNet wide-field photometric instruments (Bakos et al. 2004) between the nights of UT 2011 October 14 and UT 2012 May 3. A total of 6509 observations of a $10\overset{\circ}{.}6 \times 10\overset{\circ}{.}6$ field centered at R.A. $= 06^{\rm h}24^{\rm m}$, decl. $= +30^\circ$ were made with the HAT-6 telescope in Arizona, and 4194 observations of this same field were made with the HAT-9 telescope in Hawaii (the count is after filtering some 40 outlier measurements). We used a Sloan *r* filter and an exposure time of 180 s. Following Bakos et al. (2010) and Kovács et al. (2005), we reduced the images to trend-filtered light curves for the ∼124,000 stars in the field with $r < 14.5$ mag, achieving a point-to-point rms precision of 3.5 mmag for the brightest non-saturated stars with $r \sim 10$ mag (for HAT-P-56 the rms of the

[8] http://hatnet.org

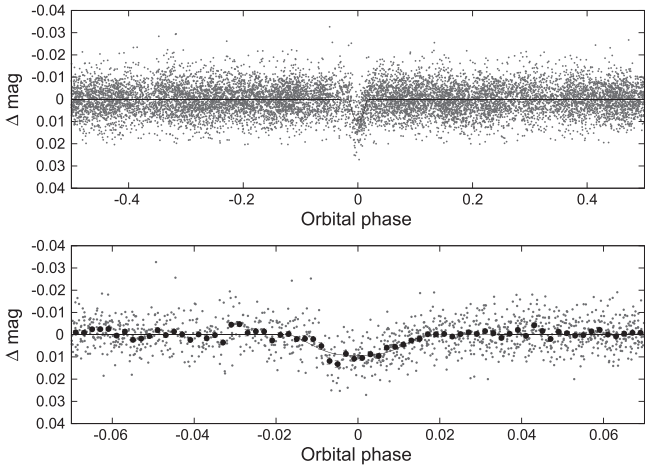

Figure 2. HATNet light curve of HAT-P-56 phase folded with the transit period. The top panel shows the unbinned light curve, while the bottom shows the region zoomed-in on the transit, with dark filled circles for the light curve binned in phase with a binsize of 0.002. The solid line shows the model fit to the light curve.

residuals from our best-fit transit model is 6.7 mmag). We searched these light curves for periodic transit signals using the Box Least Squares algorithm (BLS; Kovács et al. 2002).

A total of 29 candidate transiting planets were identified from these light curves, including HAT-P-56, whose phase-folded HATNet light curve we show in Figure 2. Reconnaissance spectroscopy and photometric follow-up observations have been carried out for most of these candidates, based on which we have rejected 21 of them as false positives. In addition to HAT-P-56, which we confirm as a planetary system in this paper, one other planet has been confirmed from this field (HAT-P-54b; Bakos et al. 2015). Six of the candidates remain active.

2.1.2. Photometric Follow-up with KeplerCam

Initial photometric follow-up observations of HAT-P-56 were carried out with KeplerCam on the FLWO 1.2 m telescope. We observed a single transit ingress on the night of UT 2013 March 25 using an *i*-band filter and an exposure time of 10 s. The images were reduced to a light curve following Bakos et al. (2010), including external parameter decorrelation (EPD) performed simultaneously with the transit fit to remove systematic trends; this trend-corrected light curve is shown in Figure 3. The rms of the residuals from our best-fit model is 2.2 mmag for these data.

2.2. Spectroscopy

We carried out spectroscopic observations of HAT-P-56 between UT 2012 October 31 and UT 2014 November 25 using the TRES (Fűresz 2008) on the 1.5 m Tillinghast Reflector at FLWO. We extracted spectra from the images and measured initial RVs, bisector spans (BSs) and stellar atmospheric parameters following Buchhave et al. (2010).

The first three TRES observations made between UT 2012 October 31 and UT 2012 November 7 using a short exposure time of 360 s resulted in a S/N per resolution element of 38–45, and were used for reconnaissance purposes. Based on these three reconnaissance spectra we found that HAT-P-56 is an F dwarf star with a fairly rapid projected rotation velocity of $\sim$40 km s^{-1}, and no evidence for additional stellar components in the spectrum. The three RV measurements were consistent with no variation above 600 m s^{-1} (3σ upper limit). A single APO 3.5 m/ARCES spectrum of HAT-P-56 was also obtained for reconnaissance on UT 2012 November 7. A 160 s exposure time was used to achieve a S/N per resolution element of 28.6. We reduced the observation to a wavelength-calibrated spectrum with the IRAF ECHELLE package[9] and used the Stellar Parameter Classification program (SPC; Buchhave et al. 2012) to measure the atmospheric parameters and radial velocity from the spectrum. This spectrum was also found to be single-lined, had an RV consistent with the TRES measurements, and also indicated that the target was a F dwarf with $v \sin i = 40$ km s^{-1}.

Following the *K2* observations (Section 2.3), which showed clean transits with no evidence of secondary eclipses or strong out-of-transit variability in phase with the transits, we resumed spectroscopic monitoring with TRES on the FLWO 1.5 m telescope, now with the aim of measuring the mass of the planet by detecting the orbital motion of the host star. A total of 18 high S/N (ranging from 50 to 113) observations were collected between UT 2014 October 2 and UT 2014 November 15. We measured stellar atmospheric parameters from these spectra using SPC, and carried out a multi-order velocity analysis following Bieryla et al. (2014) to measure the RVs relative to one of the observed spectra and spectral line BSs. Table 2 provides the measurements extracted from these spectra, where we exclude the reconnaissance spectra that were deemed to be of too low S/N to be used for our final characterization of the orbit and the stellar atmospheric properties. The phase-folded RVs and BSs are shown in Figure 4 together with our best-fit circular and eccentric orbit models. We show in Section 3.2 that the above RV measurements confirm the planet nature of HAT-P-56b.

2.3. K2 Photometry Follow Up

Encouraged by the HATNet, FLWO 1.2 m, and TRES observations, we proposed HAT-P-56 as a target for the *K2* Campaign 0 through the *Kepler* Guest Observing Program. The observations are in *Kepler* Long Cadence mode ($\sim$30 minute exposures) with a stamp size of 27×27 pixels on *Kepler* CCD Module 10, Channel 29, and were carried out between BJD 2456728.5282 and BJD 2456805.1883 (UT 2014 March 8 to UT 2014 May 27). There are two data gaps during the observation, from BJD 2456732.4309 to BJD 2456735.6386, and from BJD 2456744.1180 to BJD 2456767.5941. Module 10 is one of the outermost modules on the *Kepler* spacecraft, and as a result, the target drifted for a significant fraction of a pixel during each 30 minute exposure, leading to an elongated point-spread function (PSF). The bright neighbor 49″ away from the target is partially observed in the target "postage stamps" (see Figure 5).

The data were reduced using HATNet's reduction pipeline, certain aspects of which are described in Pál (2009). After source extraction, we measured the flux of the star in a series of circular apertures, and the sky background in circular annuli. The sky background is determined by taking the median of all the pixels with iterative outlier rejection in the annuli to

[9] IRAF is distributed by the National Optical Astronomy Observatories, which are operated by the Association of Universities for Research in Astronomy, Inc., under cooperative agreement with the National Science Foundation.

Table 2
Relative Radial Velocities, and Bisector Span Measurements of HAT-P-56

BJD[a] (2,456,900+)	RV[b] (m s^{-1})	σ_{RV} (m s^{-1})	BS (m s^{-1})	σ_{BS} (m s^{-1})	Phase	Instrument
32.99501	68	114	48.70	82.40	0.937	TRES
34.00383	−376	152	150.10	57.10	0.299	TRES
34.99731	0	54	64.40	58.30	0.655	TRES
36.00811	−310	107	2.40	45.50	0.017	TRES
42.99104	−170	70	67.10	50.00	0.519	TRES
43.98771	−268	146	−161.50	56.80	0.876	TRES
44.97264	−558	119	−57.30	70.80	0.229	TRES
46.00112	−113	102	−63.80	74.60	0.598	TRES
58.97630	−493	99	−65.60	44.80	0.247	TRES
60.02365	−221	92	−32.30	65.70	0.622	TRES
60.97679	−150	114	49.20	67.20	0.964	TRES
61.96910	−544	78	−111.70	111.00	0.319	TRES
65.96895	−80	87	−43.50	52.20	0.753	TRES
69.93743	−649	95	−2.40	69.50	0.174	TRES
70.89553	−419	153	16.40	58.90	0.518	TRES
71.85396	−187	105	85.90	80.70	0.861	TRES
72.94426	−609	54	36.40	34.10	0.252	TRES
77.04183	−331	96	−52.80	47.40	0.720	TRES

Notes.
[a] Barycentric Julian Date calculated directly from UTC, *without* correction for leap seconds.
[b] The zero-point of these velocities is arbitrary. An overall offset γ_{rel} fitted to these velocities in Section 3 has *not* been subtracted.

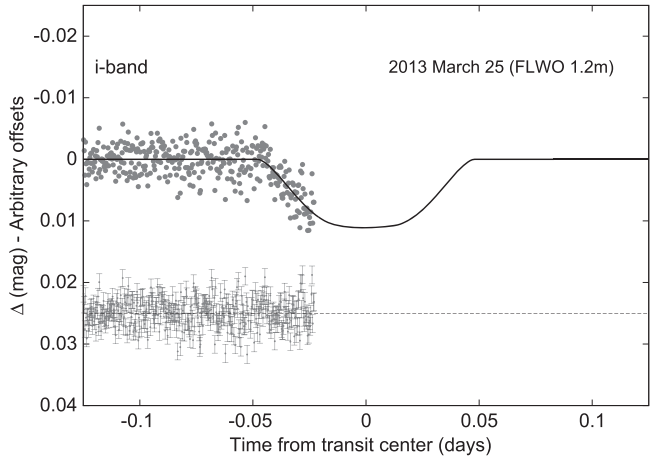

Figure 3. Unbinned transit light curve for HAT-P-56, acquired with KeplerCam at the FLWO 1.2 m telescope on the night of 2013 March 25. The light curve was corrected for trends, which were fit simultaneously with the transit model. Our best fit from the global modeling described in Section 3 is shown by the solid line. Residuals from the fit are displayed below the original light curve. The error bars represent the photon and background shot noise, plus the readout noise.

exclude the influence from the bright neighbor star. The best aperture was of 3.3 pixels radius, based on the minimum rms we achieve (shown in Figure 5 together with the background annulus we used).

To correct the photometry for variations due to the motion of the spacecraft, we performed an EPD on the extracted raw light curve. Before detrending, data points obtained during thrust fires were rejected following a similar methodology to that described in Vanderburg & Johnson (2014). We also discarded the first segment of data (from BJD 2456728.752975 to BJD 2456771.394346) obtained before the first safe mode, and the first transit right after the second safe mode while the space craft was still adjusting its pointing. We describe the systematics as a function of the x, y centroid of the star, the background flux bg, and the uncertainty of the background flux e_{bg}:

$$\begin{aligned} f(m) = c_0 &+ c_1 \sin(2\pi\, x) + c_2 \cos(2\pi\, x) \\ &+ c_3 \sin(2\pi\, y) + c_4 \cos(2\pi\, y) \\ &+ c_5 \sin(4\pi\, x) + c_6 \cos(4\pi\, x) \\ &+ c_7 \sin(4\pi\, y) + c_8 \cos(4\pi\, y) \\ &+ c_9 \mathrm{bg} + c_{10} e_{bg}. \end{aligned}$$

To preserve the signal of the transit, we modify the original EPD algorithm to only fit with the out-of-transit part of the light curve. The light curve is then detrended with cosine filters as described in Huang et al. (2013). We allowed a minimum period of 0.5 days for the filters, to preserve the transit signal.

The resulting *K2* light curve is shown in Figure 6, together with our best-fit transit model. The residuals have per-point rms of 0.17 mmag. In order to search for additional transit signals, we removed the signal of HAT-P-56b from the *K2* light curve according to the best fit transit parameters, and then reprocessed the light curve with the same detrending steps. We ran BLS on the detrended residual light curve. There is no evidence for the presence of other transits. We also conducted a grid search in phase to look for the secondary eclipse with the transit period fixed. We could not find a significant detection of the secondary eclipse. We put an 1σ upper limit of 65 ppm (0.065 mmag) on the depth of the secondary eclipse. This is estimated by computing the weighted average of the variance of points in-transit and the variance of points out-of-transit. The 1σ upper limit on the depth of the secondary eclipse we obtained from the *K2* light curve is much smaller than the predicted secondary eclipse depth (0.7 mmag) if assuming the system is a blended binary (see Section 3.3).

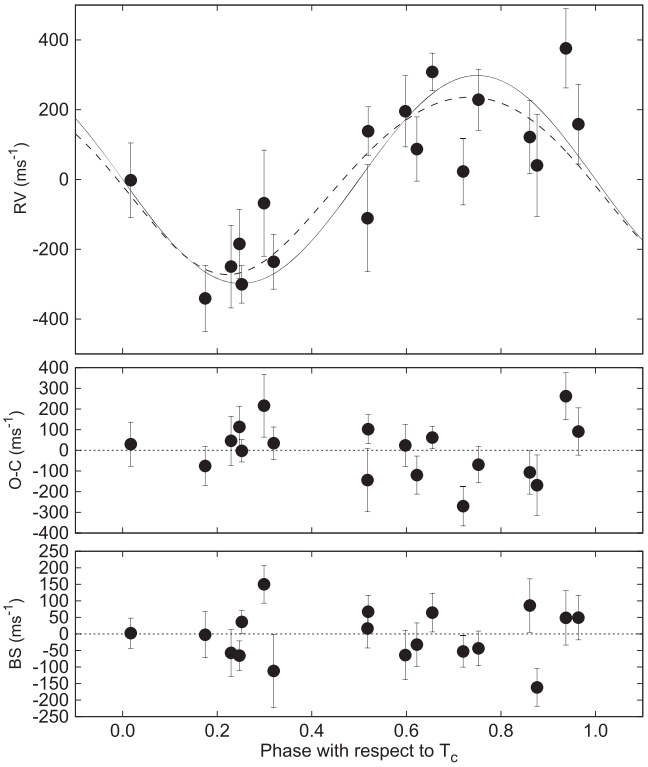

Figure 4. Top panel: RV measurements from FLWO 1.5 m/TRES shown as a function of orbital phase, along with our best-fit circular model (solid line; see Table 5), and our best-fit eccentric model (dashed line). Zero phase corresponds to the time of mid-transit. The center-of-mass velocity has been subtracted. Second panel: Velocity $O-C$ residuals from the best fit circular orbit. Third panel: Bisector spans (BS). Note the different vertical scales of the panels.

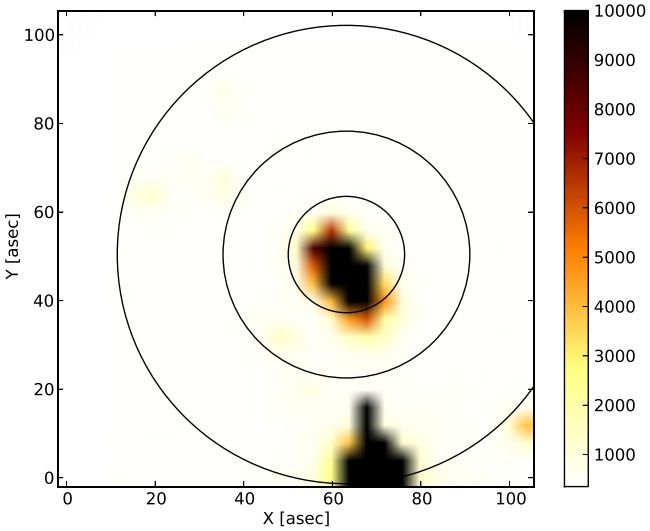

Figure 5. Image stamp from *K2* Campaign 0 containing HAT-P-56. The neighbor at 49″ away from HAT-P-56 is partially observed at the bottom of the stamp. The inner most circle indicates the optimal aperture we selected that gave the best out of transit light curve rms. The annulus between the outer two circles is used to calculate the background.

3. ANALYSIS

3.1. Stellar Parameters

The adopted stellar atmospheric parameters of HAT-P-56 are based on our SPC analysis of the 18 high S/N TRES spectra (Section 2.2 and Table 3). SPC was applied individually to each spectrum, and we take the error-weighted mean of the individual atmospheric parameter measurements. The adopted uncertainties (0.1 dex for $\log g_\star$, 50 K for $T_{\rm eff\star}$, 0.080 dex for [Fe/H] and 0.50 km s^{-1} for $v \sin i$) reflect our estimate of the systematic errors in this method based on observations of spectroscopic standard stars. Following Sozzetti et al. (2007) we combine the resulting $T_{\rm eff\star}$ and [Fe/H] measurements with the $\rho_\star$ measurements from our joint analysis of the RV and light curve data (Section 3.2), and compare them to the Yonsei-Yale stellar evolution models (Yi et al. 2001; the comparison is shown in Figure 7), to determine the physical stellar parameters (mass, radius, age, luminosity, etc.). As is often the case, we find that the resulting $\log g_\star$ value from this modeling differs significantly from that determined through our initial SPC analysis, and we therefore carried out a second iteration of SPC, fixing $\log g_\star$ to the isochrone-based value. Repeating the joint RV+light curve analysis and the stellar evolution look-up, we find that the $\log g_\star$ value had converged, and therefore did not carry out any further iterations. The final parameters that we adopt for HAT-P-56 are listed in Table 4 together with identifying information and catalog photometry. We find that the star HAT-P-56 has a mass of $1.296 \pm 0.036\,M_\odot$, a radius of $1.428 \pm 0.030\,R_\odot$, an age of 2.01 ± 0.35 Gyr, and is at a reddening-corrected distance of 310.5 ± 7.1 pc (where we use the Cardelli et al. 1989 extinction law with $R_V = 3.1$).

3.2. Global Modeling of RVs and Light Curves

We carried out a joint analysis of the TRES RVs and the HATNet, KeplerCam, and *K2* light curves following Bakos et al. (2010) with modifications described by Hartman et al. (2012). The RVs are modeled using a Keplerian orbit, while the light curves are fit with a Mandel & Agol (2002) transit model, with quadratic limb darkening coefficients adopted from Claret (2004) and Claret & Bloemen (2011). The HATNet light curve that we analyzed has been filtered via the EPD and TFA procedures before fitting the model, so we include a dilution factor to account for possible over-filtering of the transits. For the *K2* light curve, we integrate the model over the 30 minute exposure time (this is done by evaluating the model flux ratio at four evenly spaced times within a 30 minute bin, and taking the average). We used Equation (8) of Kipping & Bakos (2011a) for our *K2* model to account for a possible occultation signature and/or a variation due to reflected light (in practice we find that the light curve is consistent with no such variations). The *K2* light curve has been fitted simultaneously with the TFA algorithm using 47 template stars observed in the same channel. For the KeplerCam light curve, we use a simple model for instrumental trends (consisting of a quadratic function of time and linear functions in the PSF shape parameters), which we fit simultaneously with the physical model. We use a differential evolution Markov-chain Monte Carlo (ter Braak 2006) procedure to explore the fitness landscape and to determine the posterior parameter distributions.

The fit was performed both fixing the eccentricity to zero, and allowing it to vary. We find that the TRES RVs do prefer a slight eccentricity of $e = 0.130 \pm 0.058$, but based on the Bayesian evidence (estimated from the Markov-chain following the method of Weinberg et al. 2013), we conclude that the difference in χ^2 is not significant enough to justify the additional free parameters, and therefore we adopt the circular

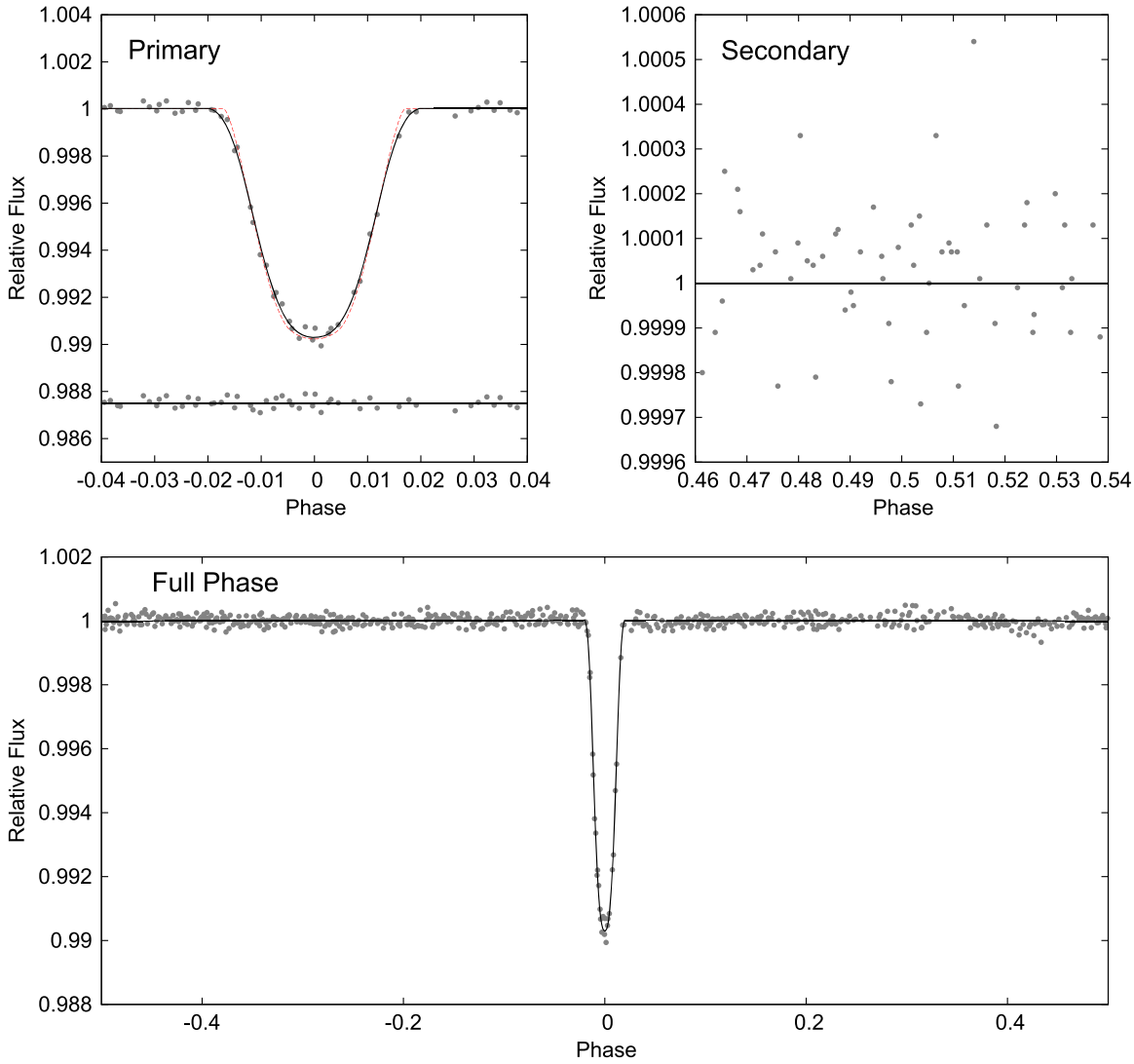

Figure 6. Phase-folded 30 minute cadence *K2* observations of HAT-P-56. The phase-folded light curve is shown in the bottom panel. In the top left we show a zoom-in on the transit, while in the top right we show a zoom-in on the expected phase of occultation assuming a circular orbit. The solid line shows our best-fit model to the observations, binned over the 30 minute integrations. The dashed line, visible only in the top-left panel, shows the model without binning.

orbit model. The 95% confidence upper limit on the eccentricity is $e < 0.246$.

Table 5 lists the adopted parameters for the planet HAT-P-56b. We find that this planet has a mass of $2.18 \pm 0.25\ M_J$, a radius of $1.466 \pm 0.040\ R_J$, and is orbiting its host star with a period of 2.7908327 ± 0.0000047 days and an orbital separation of 0.04230 ± 0.00039 AU. At this separation the planet would have an equilibrium temperature of 1840 ± 21 K assuming zero albedo and complete redistribution of heat.

3.3. Blend Analysis

In order to rule out the possibility that HAT-P-56 is a blended stellar eclipsing binary system we carried out a blend analysis following Hartman et al. (2012), with a few modifications to properly handle the *K2* light curve. These include: (1) integrating each simulated light curve model over the 30 minute exposures and using the integrated model in calculating the χ^2 difference from the observations (Kipping & Bakos 2011a); (2) using the Claret & Bloemen (2011) limb darkening coefficients for the *Kepler* band-pass; (3) using a polynomial transformation from *griz* to the *Kepler Kp* magnitude system to predict the relative fluxes of blended stars in the *Kepler* band-pass.

We find that we can rule out a blended eclipsing binary scenario with greater than 5σ confidence based solely on the photometry (including both HATNet and *K2* photometry). The *K2* data is key in making this assessment. Although blend models exist which fit the primary transit, such models predict a secondary eclipse with a depth of $\Delta K_p = 0.7$ mmag, which is ruled out by the *K2* light curve (Figure 8). Further evidence against a blend scenario is the lack of BS variations (the TRES BS measurements have an rms scatter of $77\ \mathrm{m\ s^{-1}}$) and the significant RV variation in phase with the photometric ephemeris and consistent with a transiting planet.

We also considered the possibility that HAT-P-56 is a transiting planet system with a fainter, unresolved, stellar companion. From the 2MASS catalog there are no known stars within $20''$ of HAT-P-56 with $\Delta K < 5$ mag. The highest spatial resolution observations available are our KeplerCam observations which have a PSF FWHM of $3''.5$. Based on these images

Table 3
Stellar Atmospheric Parameters for HAT-P-56 Measured with SPC

BJD[a] (2,456,900+)	$T_{\rm eff,1}$ [b] (K)	log g_1 [b] (c.g.s.)	[m/H]$_1$ [b]	$v \sin i_{\rm eff,1}$ [b] (km s^{-1})	$T_{\rm eff,2}$ [c] (K)	[m/H]$_2$ [c]	$v \sin i_{\rm eff,2}$ [c] (km s^{-1})	S/N[c]
32.99501	6406	4.01	−0.140	40.06	6545	−0.052	39.84	55.7
34.00383	6500	4.09	−0.029	40.72	6592	+0.034	40.67	56.2
34.99731	6500	4.15	−0.174	40.19	6538	−0.150	40.10	102.7
36.00811	6588	4.27	−0.103	39.83	6576	−0.116	39.87	84.0
42.99104	6528	4.17	−0.100	39.62	6572	−0.079	39.54	92.9
43.98771	6527	4.21	−0.101	40.20	6553	−0.099	40.18	83.8
44.97264	6533	4.23	−0.104	39.86	6531	−0.100	39.89	80.1
46.00112	6551	4.21	−0.095	39.75	6569	−0.091	39.74	101.6
58.97630[d]	...	...	...	...	6555	−0.071	40.38	91.9
60.02365[d]	...	...	...	...	6598	−0.057	40.15	74.9
60.97679[d]	...	...	...	...	6534	−0.109	39.59	90.6
61.96910[d]	...	...	...	...	6544	+0.062	41.80	49.3
65.96895[d]	...	...	...	...	6576	−0.082	40.03	113.2
69.93743[d]	...	...	...	...	6603	−0.077	40.02	91.9
70.89553[d]	...	...	...	...	6612	−0.083	39.80	78.6
71.85396[d]	...	...	...	...	6540	−0.093	39.88	97.6
72.94426[d]	...	...	...	...	6592	−0.123	39.59	96.5
77.04183[d]	...	...	...	...	6561	−0.099	40.03	78.4

Notes.
[a] Barycentric Julian Date calculated directly from UTC, *without* correction for leap seconds.
[b] Measurements from initial SPC iteration in which log $g_\star$ was allowed to vary.
[c] Measurements from second SPC iteration in which we fixed log $g_\star$ to 4.235.
[d] Observations were obtained after running our initial SPC analysis. They were included, however, in our fixed-log $g_\star$ SPC analysis.

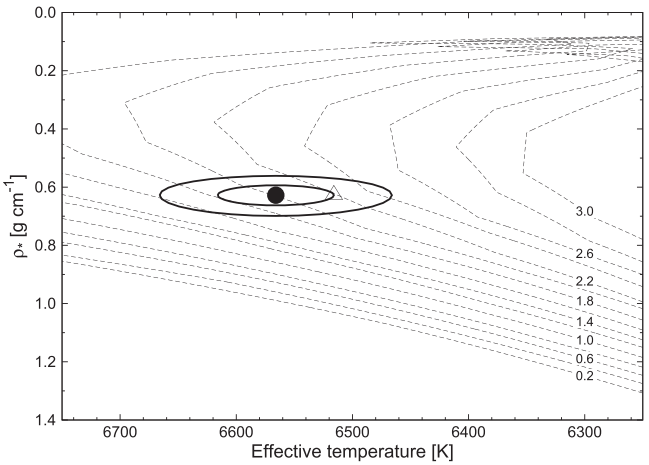

Figure 7. Comparison between the measured values of $T_{\rm eff\star}$ and $\rho_\star$ (filled circle), and the Y^2 model isochrones from Yi et al. (2001). The best-fit values, and approximate 1σ and 2σ confidence ellipsoids are shown. The open triangle shows the values from our initial SPC iteration. The Y^2 isochrones are shown for ages of 0.2–3.0 Gyr, in 0.2 Gyr increments.

we can rule out a companion with $\Delta i \lesssim 3.5$ mag to within $5''.4$. Based on our blend modeling we find that models including a stellar companion with $M > 0.67\ M_\odot$ yield a higher χ^2 value than a single star with a transiting planet, but, except for companions very close in mass to HAT-P-56b, which can be ruled out with $\gtrsim 3\sigma$ confidence, the difference in χ^2 between models with and without companions is not statistically significant. Higher spatial resolution imaging, and/or long-term RV monitoring is needed to check for a binary star companion. If such a companion exists, the mass and radius of HAT-P-56b would both be larger than what we infer here.

3.4. Out of Transit Variation of HAT-P-56

Stellar variability with amplitude ∼1 mmag are present in the *K2* light curve (see Figure 9). The Lomb–Scargle normalized power spectrum (Lomb 1976; Scargle 1982) of the star suggest that it is likely a pulsating γ Dor, with the primary period of $\sim 1.644 \pm 0.03$ days. The second strongest period peak is at $\sim 1.744 \pm 0.023$ days. The effective temperature and the surface gravity of the star place it outside the low temperature boundary of the classical instability strip, but within the range of other γ Dors discovered by the *Kepler* Mission (Uytterhoeven et al. 2011).

We tried to constrain the orbital phase variation due to HAT-P-56b with the K2 light curve. To take into account the influence of the stellar variability, we simultaneously fit for the amplitude of the six most dominant Fourier modes detected by the Lomb–Scargle algorithm, together with the expected reflection, beaming, and ellipsoid variation effects with periods constrained due to the presence of the planet. The best fitted values and error bars are presented in Table 6. We report a 3σ detection of the reflection effect, with an amplitude of 21 ± 7 ppm, which is comparable to the theoretically estimated value (27.4 ppm, following Mazeh & Faigler 2010). We do not detect the beaming effect. The ellipsoidal variation is detected with a 2σ significance. However, we caution the reader, that we also obtain a high amplitude coefficient for the $\sin(2\pi/(P_{\rm orb}/2)t_j)$ term, which indicates the detected ellipsoidal variation is not in phase with the planet transit. This could be due to our poor understanding

Table 4
Stellar Parameters for HAT-P-56

Parameter	Value	Source
Identifying Information		
R.A. (h:m:s)	$06^h43^m23^s.52$	2MASS
Decl. (d:m:s)	$+27°15'08''.2$	2MASS
GSC ID	GSC 1901-00976	GSC
2MASS ID	2MASS 06432353 +2715082	2MASS
EPIC ID	202126852	EPIC
Spectroscopic Properties		
$T_{\rm eff\star}$(K)	6566 ± 50	SPC[a]
[m/H]	−0.077 ± 0.080	SPC
$v \sin i$ (km s^{-1})	40.06 ± 0.50	SPC
$\gamma_{\rm RV}$ (km s^{-1})	35.11 ± 0.1	TRES
Photometric Properties		
B (mag)	11.287 ± 0.040	APASS
V (mag)	10.908 ± 0.036	TASS Mark IV
I (mag)	9.919 ± 0.093	TASS Mark IV
Kep (mag)	10.9	EPIC
g (mag)	11.040 ± 0.030	APASS
r (mag)	10.762 ± 0.080	APASS
i (mag)	10.709 ± 0.060	APASS
J (mag)	10.068 ± 0.021	2MASS
H (mag)	9.881 ± 0.017	2MASS
K_s (mag)	9.830 ± 0.016	2MASS
Derived Properties		
$M_\star$ ($M_\odot$)	1.296 ± 0.036	Isochrones+$\rho_\star$ +SPC[b]
$R_\star$ ($R_\odot$)	1.428 ± 0.030	Isochrones+$\rho_\star$ +SPC
$\log g_\star$ (cgs)	4.240 ± 0.015	Isochrones+$\rho_\star$ +SPC
$L_\star$ ($L_\odot$)	3.39 ± 0.19	Isochrones+$\rho_\star$ +SPC
M_V (mag)	3.411 ± 0.067	Isochrones+$\rho_\star$ +SPC
M_K (mag, ESO)	2.398 ± 0.048	Isochrones+$\rho_\star$ +SPC
Age (Gyr)	2.01 ± 0.35	Isochrones+$\rho_\star$ +SPC
A_V (mag)[c]	$0.0080^{+0.0590}_{-0.0080}$	Isochrones+$\rho_\star$ +SPC
Distance (pc)	310.5 ± 7.1	Isochrones+$\rho_\star$ +SPC
$\rho_\star$(g cm^{-3})	0.627 ± 0.033	LC[d]

Notes.
[a] SPC = "Stellar Parameter Classification" method based on cross-correlating high-resolution spectra against synthetic templates (Buchhave et al. 2012). These parameters rely primarily on SPC, but have a small dependence also on the iterative analysis incorporating the isochrone search and global modeling of the data, as described in the text.
[b] Isochrones+$\rho_\star$+SPC = Based on the Y^2 isochrones (Yi et al. 2001), the stellar density used as a luminosity indicator, and the SPC results.
[c] Total V-band extinction to the star determined by comparing the catalog broad-band photometry listed in the table to the expected magnitudes from the Isochrones+$\rho_\star$+SPC model for the star. We use the Cardelli et al. (1989) extinction law.
[d] The stellar density is determined primarily from fitting the transit light curve. There is also a slight dependency on the SPC atmospheric parameters and stellar evolution models through the adopted limb darkening coefficients.

Table 5
Parameters for the Transiting Planet HAT-P-56b

Parameter	Value[a]
Light Curve Parameters	
P (days)	2.7908327 ± 0.0000047
T_c (BJD)[b]	2456553.61645 ± 0.00042
T_{14} (days)[b]	0.09463 ± 0.00093
$T_{12} = T_{34}$ (days)[b]	0.0336 ± 0.0021
$a/R_\star$	6.37 ± 0.11
$\zeta/R_\star$ [c]	29.37 ± 0.21
$R_p/R_\star$	0.10540 ± 0.00086
b^2	$0.7613^{+0.0077}_{-0.0104}$
$b \equiv a \cos i/R_\star$	$0.8725^{+0.0044}_{-0.0060}$
i (degree)	82.13 ± 0.18
Limb-darkening Coefficients[d]	
c_1, i (linear term)	0.1716
c_2, i (quadratic term)	0.3692
c_1, r	0.2396
c_2, r	0.3825
c_1, *Kep*	0.3239
c_2, *Kep*	0.3235
RV Parameters	
K (m s^{-1})	262 ± 30
e[e]	<0.246
RV Jitter (m s^{-1})[f]	<15
Planetary Parameters	
M_p (M_J)	2.18 ± 0.25
R_p (R_J)	1.466 ± 0.040
$C(M_p, R_p)$ [g]	0.08
ρ_p (g cm^{-3})	0.86 ± 0.12
$\log g_p$ (cgs)	3.402 ± 0.055
a (AU)	0.04230 ± 0.00039
$T_{\rm eq}$ (K)[h]	1840 ± 21
Θ [i]	0.096 ± 0.011
$\langle F_j \rangle$ (10^9 erg s^{-1} cm^{-2})[j]	2.59 ± 0.12

Notes.
[a] The adopted parameters assume a circular orbit. Based on the Bayesian evidence ratio we find that this model is strongly preferred over a model in which the eccentricity is allowed to vary in the fit. For each parameter we give the median value and 68.3% (1σ) confidence intervals from the posterior distribution.
[b] Reported times are in Barycentric Julian Date calculated directly from UTC, *without* correction for leap seconds. T_c: reference epoch of mid transit that minimizes the correlation with the orbital period. T_{14}: total transit duration, time between first to last contact; $T_{12} = T_{34}$: ingress/egress time, time between first and second, or third and fourth contact.
[c] Reciprocal of the half duration of the transit used as a jump parameter in our MCMC analysis in place of $a/R_\star$. It is related to $a/R_\star$ by the expression $\zeta/R_\star = a/R_\star (2\pi(1 + e \sin\omega))/(P\sqrt{1-b^2}\sqrt{1-e^2})$ (Bakos et al. 2010).
[d] Values for a quadratic law, adopted from the tabulations by Claret (2004), Claret et al. (2013) according to the spectroscopic (SPC) parameters listed in Table 4.
[e] The 95% confidence upper-limit on the eccentricity from a model in which the eccentricity is allowed to vary in the fit.
[f] Error term, either astrophysical or instrumental in origin, added in quadrature to the formal RV errors. This term is varied in the fit assuming a prior inversely proportional to the jitter. In this case we find a preferred value of 0 for the jitter, and list the 95% confidence upper limit.
[g] Correlation coefficient between the planetary mass M_p and radius R_p determined from the parameter posterior distribution via $C(M_p, R_p) = \langle (M_p - \langle M_p \rangle)(R_p - \langle R_p \rangle) \rangle / (\sigma_{M_p} \sigma_{R_p}) \rangle$ where $\langle \cdot \rangle$ is the expectation value operator, and σ_x is the standard deviation of parameter x.
[h] Planet equilibrium temperature averaged over the orbit, calculated assuming a Bond albedo of zero, and that flux is reradiated from the full planet surface.
[i] The Safronov number is given by $\Theta = \frac{1}{2}(V_{\rm esc}/V_{\rm orb})^2 = (a/R_p)(M_p/M_\star)$ (see Hansen & Barman 2007).
[j] Incoming flux per unit surface area, averaged over the orbit.

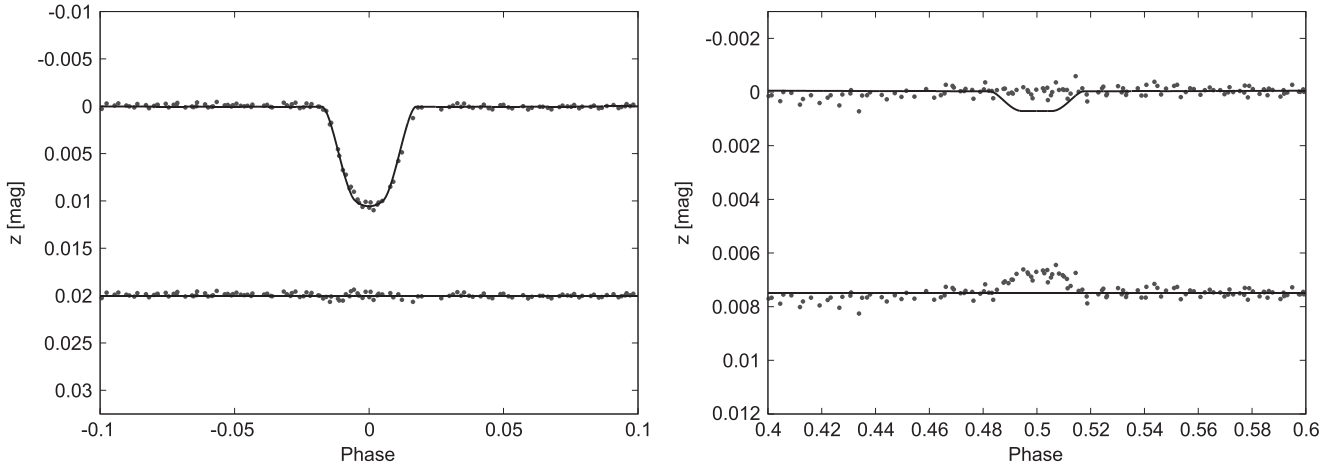

Figure 8. Comparison between the phased *K2* observations of HAT-P-56 and the predicted light curve for the best-fit blended stellar eclipsing binary model (top curve and data in each panel) together with the residuals from the model (bottom of each panel). In the left panel we show the primary eclipse, while in the right we show the secondary eclipse. The simulated primary eclipse fits the observed transit, but a significant secondary eclipse is predicted, but not observed. Note the different vertical scales in the two panels.

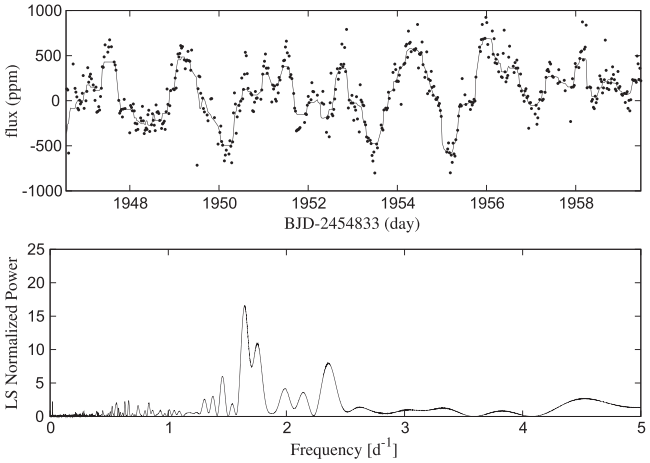

Figure 9. Top panel shows a segment of the *K2* light curve of HAT-P-56, demonstrating the out of transit variability pattern. The bottom panel shows the Lomb–Scargle normalized power spectrum of the *K2* light curve excluding the transits.

of the stellar variability, suggesting the modeled ellipsoidal variation amplitude may not be physically meaningful.

4. DISCUSSION

In this paper we presented the discovery and characterization of HAT-P-56b, an inflated massive hot Jupiter around a bright F star.

The radius anomaly of hot Jupiters is one of the oldest unsolved problems in the exoplanet field (Baraffe et al. 2010; Spiegel & Burrows 2012). Observationally, only a few very inflated planets ($R > 1.35R_J$) are observed to be above the mass of $2M_J$. It has been empirically demonstrated by various authors that more massive planets are harder to inflate. Enoch et al. (2012) derived the dependence of giant planet radius in three mass regimes, and found that the radii of high mass planets ($M > 2M_J$) are less sensitive to the equilibrium temperature of the planets, as compared to Jupiter mass planets. Weiss et al. (2013) fitted for the fundamental plane of giant planets using existing data. They found that the radius of

Table 6
Derived and Expected Orbit Phase Variation (Mazeh & Faigler 2010) for HAT-P-56 Light Curve

Coefficient	Derived Value (ppm)	Expected Value[a] (ppm)[a]	Effect
a_{1c}	-21^{+7}_{-7}	-27.4 ± 0.6	Reflection
a_{1s}	1.6^{+7}_{-7}	3.5 ± 0.4	Beaming
a_{2c}	-17^{+7}_{-7}	-6.5 ± 0.8	Ellipsoidal
a_{2s}	45^{+7}_{-7}	...	...

Note.
[a] The expected values are computed following Mazeh & Faigler (2010).

irradiated hot Jupiters inversely correlates with the planet mass. Zhou et al. (2014) investigated the mass dependence of planet radius on the equilibrium temperature, and also found that as the planet mass increase above $1M_J$, the influence on radius from irradiation decreases.

In Figure 10 we show the location of HAT-P-56b in the mass radius diagram of hot Jupiters. Taken at face value, it is the most inflated hot Jupiter with a mass in the range 1.5 M_J−4 M_J. We show the position of HAT-P-56b relative to the fundamental plane fitted by Weiss et al. (2013) in Figure 11, where it can be seen that HAT-P-56b is the farthest away from the fundamental plane when compared to the other massive planets (green points in the figure). The fundamental plane of irradiated hot Jupiters ($M > 150\,M_\oplus$, or 0.47 M_J) is expressed as the following (Weiss et al. 2013):

$$\frac{R_p}{R_\oplus} = 2.45\left(\frac{M_P}{M_\oplus}\right)^{-0.039}\left(\frac{F}{\text{erg s}^{-1}\,\text{cm}^{-2}}\right)^{0.094}.$$

The unusually large radius of HAT-P-56b, given its mass, makes it an important data point in the hot Jupiter population.

However, it is noteworthy that the radius of HAT-P-56b may have a large uncertainty due to the large impact parameter ($b = 0.8725^{+0.0044}_{-0.0060}$) indicating a nearly grazing transit. The grazing transit geometry makes the transit depth highly dependent on the limb darkening parameters of the star. The radius uncertainties are largely reduced thanks to the high

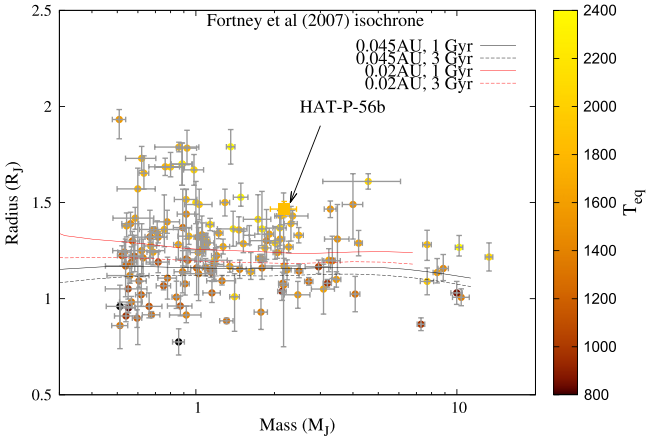

Figure 10. Mass–radius diagram for HAT-P-56b (big square) compared to the full sample of confirmed hot Jupiters (circles) from http://exoplanets.org. The points are color coded with their equilibrium temperature (cooler planets have darker colors). The error bars indicate one sigma uncertainties. The lines represents the Fortney et al. (2007) planet radius model without heavy elements cores. The black lines are for planets at 0.045 AU from a Sun like star (solid:1 Gyr, dashed:3 Gyr). The red lines are for planets at 0.02 AU from a Sun like star (solid:1 Gyr, dashed:3 Gyr).

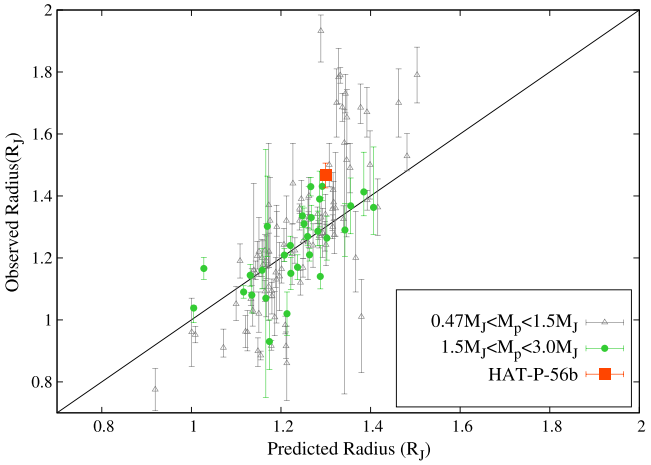

Figure 11. Observed radius of hot Jupiters vs. the radius predicted by the empirical relation of (Weiss et al. 2013). The green filled circles represent planets with mass $1.5M_J < M_p < 3.0M_J$; the light gray open triangles represent planets with mass $0.47 < M_p < 1.5M_J$. The red square is HAT-P-56b.

precision *K2* light curve. Another way to better constrain the radius of the planet would be to observe transits in the near-infrared where limb darkening is negligible. The only other planets known to be on close-to grazing orbits are TrES-2b, HAT-P-27b, WASP-34b, WASP-67b, and *Kepler*-447b (O'Donovan et al. 2006; Béky et al. 2011; Hellier et al. 2012; Mancini et al. 2014; Lillo-Box et al. 2015). While the grazing configuration increases the uncertainty of the planetary radius measurement, as Ribas et al. (2008) pointed out, such a near grazing transit has the advantage of its depth and duration being more sensitive to the presence of other planetary companions on inclined orbits. This makes HAT-P-56b a promising target among the hot Jupiters for detecting transit timing and duration variations.

Given the brightness of the host star ($V_{mag} = 10.9$), HAT-P-56 is a system of particular interest for measuring the spin–orbit obliquity angle. The estimated RM effect amplitude ΔV_R is $\sim$140 m s^{-1} following Equation (5) of Gaudi & Winn (2007). HAT-P-56 is a relatively fast rotating F star with effective temperature (6566 $\pm$ 50 K) slightly above the Albrecht et al. (2012) division for tidal alignment of hot Jupiters. Measurement of the spin–orbit obliquity will contribute an important data point to the obliquity distribution statistics. The rotation of HAT-P-56 is similar to CoRoT-11, and rapid enough that the distortion in the spectral line profiles during transit may be resolved, enabling transit Doppler tomography of the system (Collier Cameron et al. 2010; Gandolfi et al. 2012). Similar to CoRoT-11, the rotation period of HAT-P-56 is faster than the orbit period of HAT-P-56b, which is unusual (Walkowicz & Basri 2013). This may either suggest that the tidal interaction between the star and planet is weak, or the planet might be pushed out by the tides of the star from a closer orbit.

We thank the referee for useful comments. HATNet operations have been funded by NASA grants NNG04GN74G and NNX13AJ15G. Follow-up of HATNet targets has been partially supported through NSF grant AST-1108686. G.Á.B., Z.C., and K.P. acknowledge partial support from NASA grant NNX09AB29G. K.P. acknowledges support from NASA grant NNX13AQ62G. We also acknowledge partial support from the *Kepler* Mission under NASA Cooperative Agreement NNX13AB58A (D.W.L., PI). Data presented in this paper are based on observations obtained at the HAT station at the Submillimeter Array of SAO, and the HAT station at the Fred Lawrence Whipple Observatory of SAO. The authors wish to recognize and acknowledge the very significant cultural role and reverence that the summit of Mauna Kea has always had within the indigenous Hawaiian community. We are most fortunate to have the opportunity to conduct observations from this mountain. This paper presents observations made with the Apache Point Observatory 3.5 m telescope, which is owned and operated by the Astrophysical Research Consortium. The *K2* data presented in this paper were obtained from the Mikulski Archive for Space Telescopes (MAST). STScI is operated by the Association of Universities for Research in Astronomy, Inc., under NASA contract NAS5-26555. Support for MAST for non-*HST* data is provided by the NASA Office of Space Science via grant NNX09AF08G and by other grants and contracts. This paper includes data collected by the *Kepler* telescope. Funding for the *K2* Mission is provided by the NASA Science Mission directorate.

REFERENCES

Albrecht, S., Winn, J. N., Johnson, J. A., et al. 2012, ApJ, 757, 18
Bakos, G., Noyes, R. W., Kovács, G., et al. 2004, PASP, 116, 266
Bakos, G. Á, Csubry, Z., Penev, K., et al. 2013, PASP, 125, 154
Bakos, G. Á, Hartman, J. D., Bhatti, W., et al. 2015, AJ, 149, 149
Bakos, G. Á, Torres, G., Pál, A., et al. 2010, ApJ, 710, 1724
Baraffe, I., Chabrier, G., & Barman, T 2010, RPPh, 73, 016901
Barclay, T., Huber, D., Rowe, J. F., et al. 2012, ApJ, 761, 53
Batalha, N. M., Borucki, W. J., Bryson, S. T., et al. 2011, ApJ, 729, 27
Béky, B., Bakos, G. Á, Hartman, J., et al. 2011, ApJ, 734, 109
Bieryla, A., Hartman, J. D., Bakos, G. Á., et al. 2014, AJ, 147, 84
Borucki, W. J., Koch, D., Jenkins, J., et al. 2009, Sci, 325, 709
Brown, D. J. A., Anderson, D. R., Armstrong, D. J., et al. 2014, arXiv:1412.7761
Buchhave, L. A., Bakos, G. Á, Hartman, J. D., et al. 2010, ApJ, 720, 1118
Buchhave, L. A., Latham, D. W., Johansen, A., et al. 2012, Natur, 486, 375
Cardelli, J. A., Clayton, G. C., & Mathis, J. S. 1989, ApJ, 345, 245
Carter, J. A., Agol, E., Chaplin, W. J., et al. 2012, Sci, 337, 556
Claret, A. 2004, A&A, 428, 1001
Claret, A., & Bloemen, S. 2011, A&A, 529, A75
Claret, A., Hauschildt, P. H., & Witte, S. 2013, A&A, 552, A16

Collier Cameron, A., Bruce, V. A., Miller, G. R. M., Triaud, A. H. M. J., & Queloz, D. 2010, MNRAS, 403, 151
Deming, D., Sada, P. V., Jackson, B., et al. 2011, ApJ, 740, 33
Enoch, B., Collier Cameron, A., & Horne, K. 2012, A&A, 540, A99
Fortney, J. J., Marley, M. S., & Barnes, J. W. 2007, ApJ, 659, 1661
Fűresz, G. 2008, PhD thesis, Univ. of Szeged
Gandolfi, D., Collier Cameron, A., Endl, M., et al. 2012, A&A, 543, L5
Gaudi, B. S., & Winn, J. N. 2007, ApJ, 655, 550
Gautier, T. N., III, Charbonneau, D., Rowe, J. F., et al. 2012, ApJ, 749, 15
Hansen, B. M. S., & Barman, T. 2007, ApJ, 671, 861
Hartman, J. D., Bakos, G. Á, Béky, B., et al. 2012, AJ, 144, 139
Hellier, C., Anderson, D. R., Collier Cameron, A., et al. 2012, MNRAS, 426, 739
Howell, S. B., Sobeck, C., Haas, M., et al. 2014, arXiv:1402.5163
Huang, X., Bakos, G. á., & Hartman, J. D. 2013, MNRAS, 429, 2001
Jackson, B. K., Lewis, N. K., Barnes, J. W., et al. 2012, ApJ, 751, 112
Kipping, D., & Bakos, G. 2011a, ApJ, 730, 50
Kipping, D., & Bakos, G. 2011b, ApJ, 733, 36
Kovács, G., Bakos, G., & Noyes, R. W. 2005, MNRAS, 356, 557
Kovács, G., Zucker, S., & Mazeh, T. 2002, A&A, 391, 369
Lillo-Box, J., Barrado, D., Santos, N. C., et al. 2015, arXiv:1502.03267
Lissauer, J. J., Fabrycky, D. C., Ford, E. B., et al. 2011, Natur, 470, 53
Lomb, N. R. 1976, Ap&SS, 39, 447
Mancini, L., Southworth, J., Ciceri, S., et al. 2014, A&A, 568, A127
Mandel, K., & Agol, E. 2002, ApJL, 580, L171
Marcy, G. W., Isaacson, H., Howard, A. W., et al. 2014, ApJS, 210, 20
Masuda, K. 2015, arXiv:1503.05446
Mazeh, T., & Faigler, S. 2010, A&A, 521, L59
Morris, B. M., Mandell, A. M., & Deming, D. 2013, ApJL, 764, L22
Mullally, F., Coughlin, J. L., Thompson, S. E., et al. 2015, arXiv:1502.02038
O'Donovan, F. T., Charbonneau, D., Mandushev, G., et al. 2006, ApJL, 651, L61
Pál, A. 2009, PhD thesis, Department of Astronomy, Eötvös Loránd Univ.
Pál, A., Bakos, G. Á, Torres, G., et al. 2008, ApJ, 680, 1450
Pepper, J., Pogge, R. W., DePoy, D. L., et al. 2007, PASP, 119, 923
Pollacco, D. L., Skillen, I., Collier Cameron, A., et al. 2006, PASP, 118, 1407
Ribas, I., Font-Ribera, A., & Beaulieu, J.-P. 2008, ApJL, 677, L59
Sanchis-Ojeda, R., & Winn, J. N. 2011, ApJ, 743, 61
Scargle, J. D. 1982, ApJ, 263, 835
Sozzetti, A., Torres, G., Charbonneau, D., et al. 2007, ApJ, 664, 1190
Spiegel, D. S., & Burrows, A. 2012, ApJ, 745, 174
ter Braak, C. J. F. 2006, Statistics and Computing, 16, 239
Uytterhoeven, K., Moya, A., Grigahcène, A., et al. 2011, A&A, 534, A125
Vanderburg, A., & Johnson, J. A. 2014, PASP, 126, 948
Walkowicz, L. M., & Basri, G. S. 2013, MNRAS, 436, 1883
Weinberg, M. D., Yoon, I., & Katz, N. 2013, arXiv:1301.3156
Weiss, L. M., Marcy, G. W., Rowe, J. F., et al. 2013, ApJ, 768, 14
Welsh, W. F., Orosz, J. A., Seager, S., et al. 2010, ApJL, 713, L145
Wu, Y., & Lithwick, Y. 2013, ApJ, 772, 74
Yi, S., Demarque, P., Kim, Y.-C., et al. 2001, ApJS, 136, 417
Zhou, G., Bayliss, D., Penev, K., et al. 2014, AJ, 147, 144
Zhu, W., Huang, C. X., Zhou, G., & Lin, D. N. C. 2014, ApJ, 796, 67